MOLECULAR BIOLOGY

Identification and architecture of a putative secretion tube across mycobacterial outer envelope

Xiaoying Cai[1†], Lei Liu[2†], Chunhong Qiu[1†‡], Chongzheng Wen[2], Yao He[3,4], Yanxiang Cui[3], Siyu Li[1], Xuan Zhang[5], Longhua Zhang[1], Changlin Tian[1], Lijun Bi[6], Z. Hong Zhou[3,4]*, Weimin Gong[1,2]*

Tuberculosis-causing mycobacteria have thick cell-wall and capsule layers that are formed from complex structures. Protein secretion across these barriers depends on a specialized protein secretion system, but none has been reported. We show that *Mycobacterium tuberculosis* Rv3705c and its homologous MSMEG_6251 in *Mycobacterium smegmatis* are tube-forming proteins in the mycobacterial envelope (TiME). Crystallographic and cryo-EM structures of these two proteins show that both proteins form rotationally symmetric rings. Two layers of TiME rings pack together in a tail-to-tail manner into a ring-shaped complex, which, in turn, stacks together to form tubes. *M. smegmatis* TiME was detected mainly in the cell wall and capsule. Knocking out the TiME gene markedly decreased the amount of secreted protein in the *M. smegmatis* culture medium, and expression of this gene in knocked-out strain partially restored the level of secreted protein. Our structure and functional data thus suggest that TiME forms a protein transport tube across the mycobacterial outer envelope.

INTRODUCTION

The millennium-old disease, consumption [also called tuberculosis (TB)], continually plagued human societies, politics, and literature from the dawn of humanity to the advent of streptomycin in the 1940s (*1*, *2*). In recent years, TB has re-galvanized headlines because of the emergence of drug-resistant *Mycobacterium tuberculosis* strains (*3*) and numerous TB cases brought about by the rampage of the AIDS epidemic (*4*). Even today, TB remains the most prominent cause of death by a single infectious agent. Distinct from both Gram-positive and Gram-negative bacteria, mycobacteria fashion a thick and complex cell envelope (*5*–*7*), with an external capsule ~35 nm thick (*5*, *7*) and a cell wall ~14 nm thick (*8*) in addition to a normal internal lipid bilayer membrane (*7*). From inside out, the mycobacterial cell wall is made up of three covalently linked layers—a peptidoglycan layer, an arabinogalactan mesh, and mycolic acid layer—surrounded noncovalently by a layer of glycolipid (*6*, *7*). These unusual covalently linked layers of the cell wall represent a permeation barrier (*6*, *7*). Channels through the mycobacterial cell envelope contribute to mycobacterial pathogenesis by secreting virulence factors (*9*, *10*) and promoting antibiotic efflux (*11*); thus, they are targets for therapeutic intervention. However, secretion channels penetrating either the cell wall or the capsule of mycobacteria have yet to be discovered and might be better targets because of their uniqueness.

Rv3705c is an *M. tuberculosis* protein located on the cell envelope of *M. tuberculosis* H37Rv (*12*) and a potential drug target against TB (*13*). It is conserved in both gene loci and sequence in mycobacteria (fig. S1). A segment of this protein has been found to interact with target cells specifically and could inhibit *M. tuberculosis* H37Rv infection through competition (*12*). In this study, by combining x-ray crystallography and cryo–electron microscopy (cryo-EM), we obtained ring-shaped structures of Rv3705c and homologous MSMEG_6251 in *Mycobacterium smegmatis*, both of which stack into tubes in vitro. In vivo subcellular localization result shows that MSMEG_6251 is located on the cell wall and capsule. Moreover, the amount of secreted protein markedly decreased after knocking out *msmeg_6251*, while the decreased protein level was partially restored in the complemented strain. Our results support the idea that Rv3705c and MSMEG_6251 are tube-forming proteins in the mycobacterial envelope (hereafter referred to as mtTiME and msTiME, respectively) for protein secretion.

RESULTS

Soluble domain of TiME oligomerizes to form a ring-shaped structure

We set out to determine the atomic structures of mtTiME and msTiME by both x-ray crystallography and cryo-EM. Although full-length proteins were overexpressed in *Escherichia coli*, only those isolated from the cell membrane remained full length (TiME-FL; Fig. 1A) and those purified from the soluble fraction were determined to be cleaved at their N termini, resulting in the TiME soluble domain (TiME-SD; Fig. 1A). The ratio of purified TiME-SD over TiME-FL is about 30 to 40. The N-terminal segment before residue 26/28 (numbered in mtTiME-FL/msTiME-FL) was predicted to be a general secretion (Sec)–specific signal peptide. At the end of this signal peptide, we observed an AXA motif (fig. S1B) that is recognized and cleaved by type I signal peptidase (*14*). The N-terminal signal peptides of both proteins are highly hydrophobic [hydrophobicity level (*15*) >1.5 in the scale from −2 to 2] and predicted to form a transmembrane helix (designated as α0 in Fig. 1A). In this study, we were able to obtain crystals for both mtTiME-SD and msTiME-SD.

We solved the crystal structures of mtTiME-SD and msTiME-SD at 3.3- and 1.5-Å resolutions, respectively. With the root mean square deviation of 0.67 Å for all C_α atoms, the monomer structures of

[1]School of Life Sciences, University of Science and Technology of China, Hefei, Anhui, China. [2]Hefei National Laboratory for Physical Sciences at the Microscale, University of Science and Technology of China, Hefei, Anhui, China. [3]California NanoSystems Institute, University of California, Los Angeles (UCLA), Los Angeles, CA 90095, USA. [4]Department of Microbiology, Immunology and Molecular Genetics, UCLA, Los Angeles, CA 90095, USA. [5]Institute of Health Science, Institutes of Physical Science and Information Technology, Anhui University, Hefei, Anhui, China. [6]Institute of Biophysics, Chinese Academy of Sciences, Beijing, China.
*Corresponding author. Email: wgong@ustc.edu.cn (W.G.); hong.zhou@ucla.edu (Z.H.Z.)
†These authors contributed equally to this work.
‡Present address: Institute of Molecular Biology and Biophysics, ETH Zürich, Otto-Stern-Weg 5, HPK, CH-8093 Zürich, Switzerland.

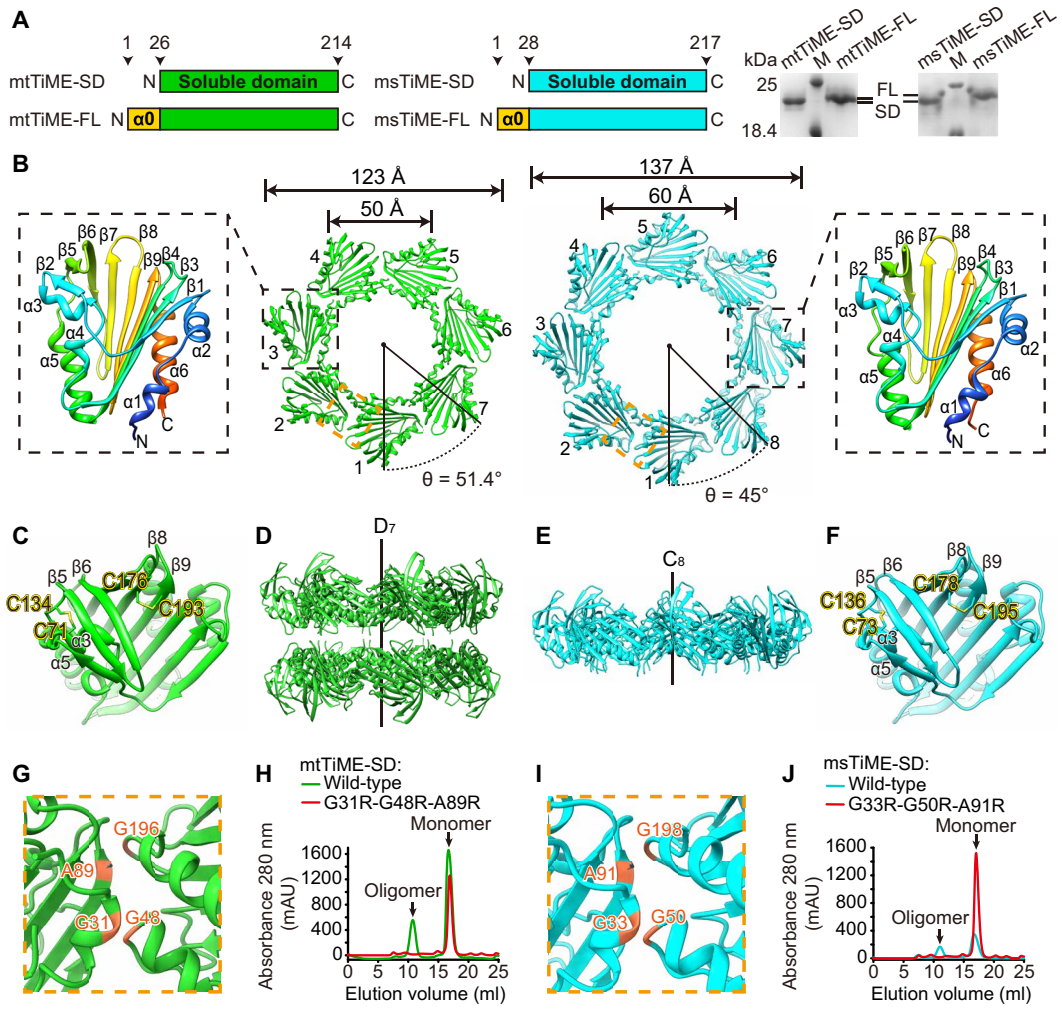

Fig. 1. Ring-shaped crystal structures of homologous proteins mtTiME-SD and msTiME-SD. (**A**) Difference between TiME-FL and TiME-SD. In proposed domain organizations (left), TiME-FL has an N-terminal helix α0 (gold), which was predicted to be a Sec-specific signal peptide by SignalP 5.0 and a transmembrane helix by TMHMM 2.0. Molecular weight gap between TiME-FL and TiME-SD is shown in SDS–polyacrylamide gel electrophoresis (SDS-PAGE) gels (right). M, molecular weight markers. (**B**, **D**, and **E**) Ribbon representation of the ring-shaped mtTiME-SD (green) and msTiME-SD (cyan) crystal structures viewed from the top (B) and side (D and E). In top views (B), one monomer from each structure is enlarged and shown as rainbow color from N-terminal blue to C-terminal red, and the rotation of one monomer to neighboring monomer is given, shown as θ. (**C** and **F**) Conserved two intramolecular disulfide bonds of mtTiME-SD (C) and msTiME-SD (F) monomers. (**G** and **I**) Enlarged and tilted views of the monomer-monomer interfaces with the conserved residues (orange) forming the interface. (**H** and **J**) TiME-SD size exclusion chromatograms of wild-type and interface disrupting mutant. mAU, micro absorbance units.

mtTiME-SD and msTiME-SD are essentially the same (Fig. 1B and fig. S2A), consistent with their highly conserved sequences (70% sequence identity; fig. S1B). Each monomer has a globular, single-domain appearance and is characterized by a twisted nine-stranded antiparallel β sheet, sandwiched by two sets of three helices (Fig. 1B). This structure is constrained by two intramolecular disulfide bonds, one between C71/73 (numbered in mtTiME-FL/msTiME-FL) and C134/136 and the other between C176/178 and C193/195 (Fig. 1, C and F). Because these four cysteine residues are highly conserved in TiME proteins of mycobacteria (fig. S1B), we believe that the two intramolecular disulfide bonds are essential for stabilizing the monomer structure of TiME proteins.

Quaternary structures in the mtTiME-SD and msTiME-SD crystals show high similarity as well (Fig. 1B and fig. S2B). The crystallized mtTiME-SD formed a double-layered ring-shaped complex of ~123 Å outer diameter and ~50 Å inner diameter with sevenfold dihedral (D_7) symmetry (Fig. 1, B and D), while msTiME-SD was crystalized in a different space group and formed a single-layered ring of ~137 Å outer diameter and ~60 Å inner diameter with eightfold (C_8) symmetry (Fig. 1, B and E). The angular rotations between neighboring monomers within the single-layered rings differ by only 6.4° in these two crystal structures (Fig. 1B). Other than these differences, the monomer-monomer interface within the single-layered rings is identical. G31/33 (numbered in mtTiME-FL/msTiME-FL) and A89/91 in one monomer interact with G48/50 and G196/198 in the neighboring monomer by hydrophobic force (Fig. 1, B, G, and I). These interactions were confirmed by mutations of G31/33R, G48/50R, and A89/91R, which prevented mtTiME-SD and msTiME-SD from forming oligomers in solution (Fig. 1, H and J, and fig. S3). The observed ring structure of TiME-SD and the propensity of the

N-terminal segment to fold into transmembrane helix α0 together suggest that the full-length protein likely oligomerizes to form a pore on cell membrane.

TiME rings pack together in a tail-to-tail manner

To determine the structure of the full-length protein, we purified mtTiME-FL from cell membrane and reconstituted it in amphipol A8-35 for cryo-EM single-particle analysis (Fig. 2, A to E, and fig. S4, A and B). Two-dimensional (2D) class averages of top-view particles show that mtTiME-FL particles exist in two forms: a major class with eightfold symmetry and a minor class with sevenfold symmetry (Fig. 2D); the particles observed from their side view (fig. S4C) indicate that the C_8 or C_7 rings stack into double-layered complex with D_8 or D_7 symmetry, respectively. Moreover, size exclusion chromatography coupled to multiangle light scattering (SEC-MALS) demonstrated that the molecular weight of mtTiME-SD oligomer in solution is 338.1 kDa, which is about 16-fold of monomer molecular weight of 21.4 kDa (Fig. 2G). Therefore, although mtTiME can form D_8 or D_7 complex in solution, the D_8 form should be the major population and was selected for further cryo-EM analysis.

We subsequently obtained a cryo-EM reconstruction of mtTiME-FL complex with D_8 symmetry at 4.4-Å resolution (fig. S4, D to F). Fitting of the crystal structures of mtTiME-SD monomer into the cryo-EM reconstruction (Fig. 2, B and C) shows that the two

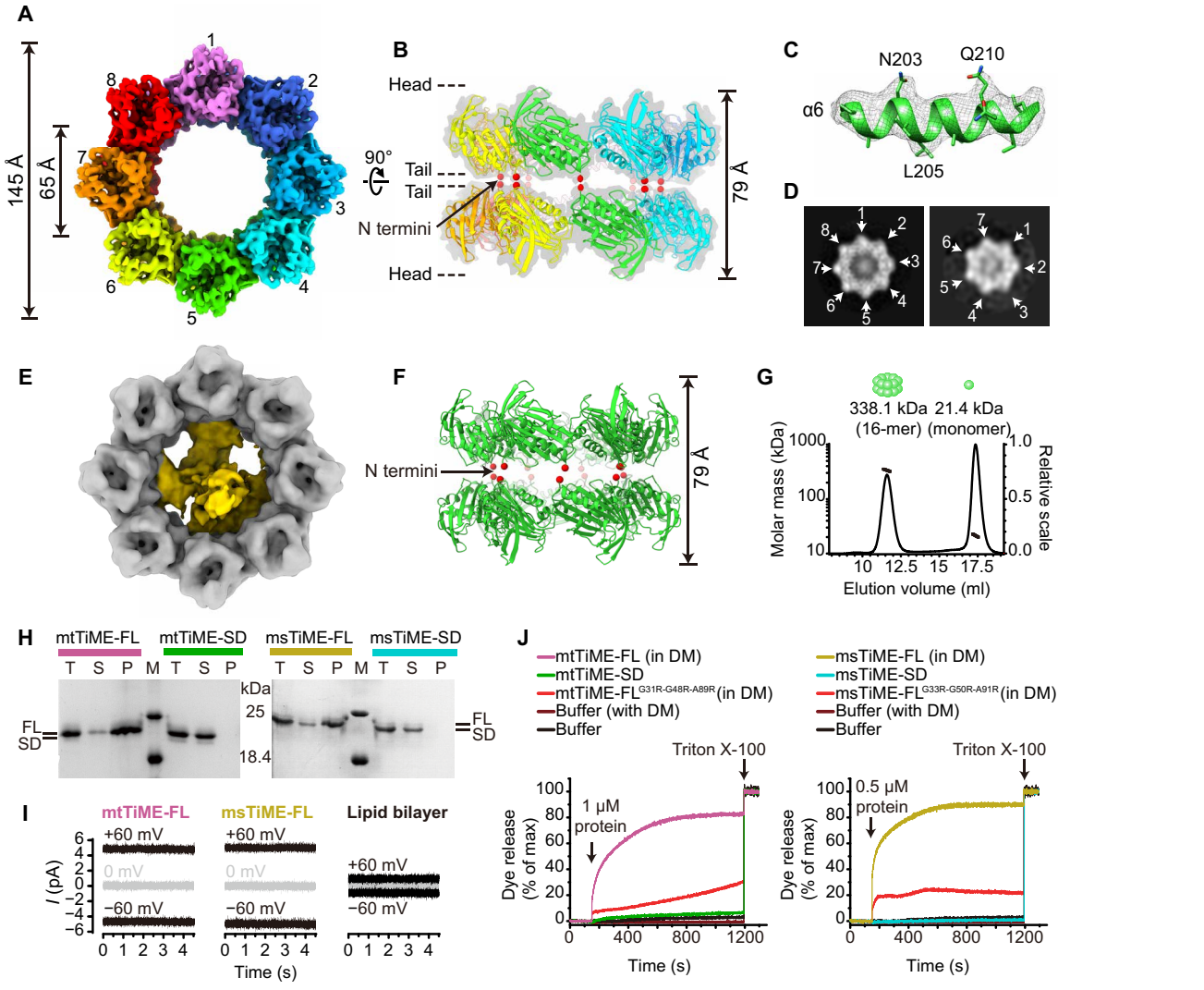

Fig. 2. Cryo-EM structure of mtTiME-FL D_8 ring-shaped complex and pore formation of TiME-FL. (**A** and **B**) Cryo-EM density map of amphipol-solubilized mtTiME-FL reconstructed by D_8 symmetry in top view (A) and side view (B). mtTiME-SD monomer crystal structures (rainbow-colored ribbons) fitted well into the density map (B). The N terminus of each mtTiME-SD monomer is marked as red sphere. (**C**) Close-up view of the density map (mesh) of helix α6 superposed with its crystal structure (green ribbon or sticks) in mtTiME-SD. (**D**) Different 2D class averages for top views of amphipol-solubilized mtTiME-FL particles showing seven and eight monomers (pointed by arrows), respectively. (**E**) mtTiME-FL cryo-EM density map reconstructed by C_1 symmetry. (**F**) Side view of double-layered mtTiME-SD tetradecameric crystal structure. (**G**) Molecular weights of mtTiME-SD with two states are determined by SEC-MALS. Short solid lines correspond to the average molecular weight distributions across each peak. (**H**) Liposome-binding assay of TiME-FL and TiME-SD. Dialysate of total proteins (T) was subjected to ultracentrifugation to isolate the supernatant fraction (S) and the precipitate fraction (P). (**I**) Representative single-channel current traces of mtTiME-FL and msTiME-FL. The recording voltage was marked above each trace. (**J**) 5(6)-Carboxyfluorescein–loaded liposomes were treated with TiME-FL, TiME-SD, and TiME-FL mutants, and dye efflux was monitored over time. *n*-Decyl-β-D-maltopyranoside (DM) concentration is the same in wild-type and mutant samples of TiME-FL. Results of (H) to (J) are representative of at least three independent biological replicates.

octameric rings in the complex are stacked together, in which two opposing monomers in the two rings are related by 36° rotation with their N termini coming together in a tail-to-tail manner (Fig. 2B and fig. S5A). Within the double-layered complex, residues H26 and E184 in the monomers of one layer are in close proximity of the same residues in the monomers of the other layer, suggesting possible interactions coordinated by ions. The tail-to-tail stacking observed in the D_8 cryo-EM reconstruction is the same as those seen in the crystal of D_7 mtTiME-SD (Fig. 2F), except for a slight difference in the angular rotation of the two opposing monomers (38° versus 36°) (fig. S5). Although only unstacked ring was seen in the msTiME-SD crystal (Fig. 1E), the C_8 msTiME-SD ring structure fits perfectly with the ring-shaped structure of the D_8 mtTiME-FL cryo-EM reconstruction (fig. S6, A and B). These observations suggest that both heptameric and octameric rings are physiologically relevant and both likely exist as double-layered, tail-to-tail stacked complexes in solution.

To visualize the N-terminal segment with propensity to become transmembrane helix α0 in mtTiME-FL, we relaxed the D_8 symmetry in our workflow and obtained an asymmetric (i.e., C_1) reconstruction of mtTiME-FL at 6.2-Å resolution (fig. S4, D, E, and G). This C_1 reconstruction can accommodate 16 copies of the mtTiME-SD crystal structure in a D_8 symmetric complex that encircles less ordered (i.e., lower resolution), asymmetric density (Fig. 2E and fig. S6, C to E). This central density is attributed to the N-terminal segment of mtTiME-FL, albeit no helix can be discerned within it (fig. S6, C and E). This observation indicates that the N-terminal fragment does not fold into a stable helix under the experimental environment of amphipol surfactant.

To overcome the limitation of amphipol surfactant and probe whether TiME-FL ring could form pore on the lipid bilayer membrane, we resorted to liposome-binding and single-channel recording assays. mtTiME-FL and msTiME-FL were successfully reconstituted in the lipid bilayer of liposomes (Fig. 2H and fig. S7, A and B). Using symmetrical electrolyte buffers and a voltage potential of +60 mV or −60 mV, the single-channel current recorded on mtTiME-FL or msTiME-FL reconstituted planar lipid bilayer was four to five times higher than the current recorded on planar lipid bilayer alone (Fig. 2I), demonstrating pore-forming effect of these two proteins. The single-channel current of TiME-FL showed no open-close fluctuation or oriented rectification (fig. S7C), indicating that the pores formed by these two proteins were kept consistently open at potential from −60 mV to +60 mV. Furthermore, 5(6)-carboxyfluorescein (CF) leakage assay validated the pore-forming activities of TiME-FL rings. CF (~10 Å) passed readily through mtTiME-FL and msTiME-FL pores from CF-loaded liposome (Fig. 2J and fig. S7D), and mutations for disrupting the monomer interface of rings described above resulted in about 63 and 76% reduction of CF leakage in mtTiME-FL and msTiME-FL, respectively (Fig. 2J). Moreover, TiME-SD could not be inserted into lipid bilayer and form pores (Fig. 2, H and J), suggesting that N-terminal helix α0 of TiME-FL is required for transmembrane pore formation. Together, these experiments establish that TiME-FL forms a transmembrane pore on lipid bilayer membrane that allowed passage of molecules of 10 Å in size.

TiME forms tubes in vitro and is localized to the mycobacterial envelope

msTiME-FL reconstituted in amphipol formed a tubular structure stacked with even-numbered rings, ranging from 10 to 20 layers (Fig. 3A and fig. S8A). Their outer diameters (Fig. 3B) and the tail-to-tail double-layered stacking as indicated by interlayer distance measurements (Fig. 3, B to D) are consistent with those observed in the D_8 cryo-EM reconstruction of mtTiME-FL in amphipol described above. Similarly, cryo-EM images of msTiME-SD (Fig. 3A) and EM images of negatively stained mtTiME-SD (Fig. 3E) reveal tubular structures of stacked double-layered complexes of the same size. mtTiME-FL in the absence of any surfactant or amphipathic molecule also forms tube-like structure (Fig. 3E). D145-G146 in mtTiME or N147-F148 in msTiME are the residues located in the projection loop at the head of TiME single-layered ring (fig. S8, C to E) and might be involved in stacking double-layered complexes to form tubes. Double mutant (D145R-G146R in mtTiME or N147R-F148R in msTiME) disrupted tube formation of TiME-SD (fig. S8, F to I), confirming that these residues are important for tube formation. These observations indicate that the tube formation property is conserved in TiME proteins and that the tube is formed by stacking double-layered complexes in a head-to-head manner (Fig. 3F).

Given TiME's property of self-assembling into tubes, we hypothesized that the tube of tens of nanometers length may span the mycobacterial cell envelope. mtTiME has been detected on the cell wall and plasma membrane of *M. tuberculosis* (*12*), and msTiME was more than threefold abundant in the cell wall of *M. smegmatis* than in the plasma membrane (*16*). To investigate whether the TiME protein is also located on the mycobacterial capsule, we isolated the capsule, cell wall, and plasma membrane fractions from *M. smegmatis* mc^2155 and probed the existence of msTiME in these fractions by Western blot. Meanwhile, we performed the same experiments with these fractions isolated from Δ*mstime M. smegmatis* mc^2155 mutant (fig. S9, A to C) as controls. As shown before (*16*), our data confirmed that the abundance of msTiME in the plasma membrane is lower than that in the cell wall (Fig. 3G). msTiME was also detected in the capsule fraction of wild-type *M. smegmatis*, while none of msTiME was detected in this fraction of Δ*mstime* mutant (Fig. 3G). Therefore, msTiME distributes on the cell envelope of *M. smegmatis*, with higher abundance in the capsule and cell wall and lower abundance in the plasma membrane.

msTiME tube is involved in protein secretion of *M. smegmatis*

Tubular msTiME's residing across *M. smegmatis* cell wall and capsule hints that it may function for protein secretion. The inner diameters of TiME-SD heptamer and octamer are 50 and 60 Å, respectively (Fig. 1B). These diameters are similar to those of GspD, VirB7-VirB9-VirB10 complex, Hcp, and CsgG, which are outer membrane porins in some secretion systems (fig. S10) and are wide enough for secreting proteins.

To test whether msTiME is involved in protein secretion, we compared the protein compositions in the culture filtrates from wild-type and Δ*mstime M. smegmatis* mc^2155 by SDS–polyacrylamide gel electrophoresis (SDS-PAGE) and label-free quantitative mass spectrometry, which was calibrated by mRNA levels. SDS-PAGE results showed that, among others, the amount of proteins below the major band at a molecular weight of ~22 kDa (indicated by * in Fig. 3H) decreased in the Δ*mstime* culture medium (Fig. 3H). Among the proteins detected by quantitative mass spectrometry, 74 had been identified to be secreted proteins experimentally (data S1) (*14*, *17*–*24*). The abundance of most of these secreted proteins decreased notably in the Δ*mstime* culture medium (58 proteins by >2-fold, 40 proteins by >10-fold, 31 proteins by >20-fold, and

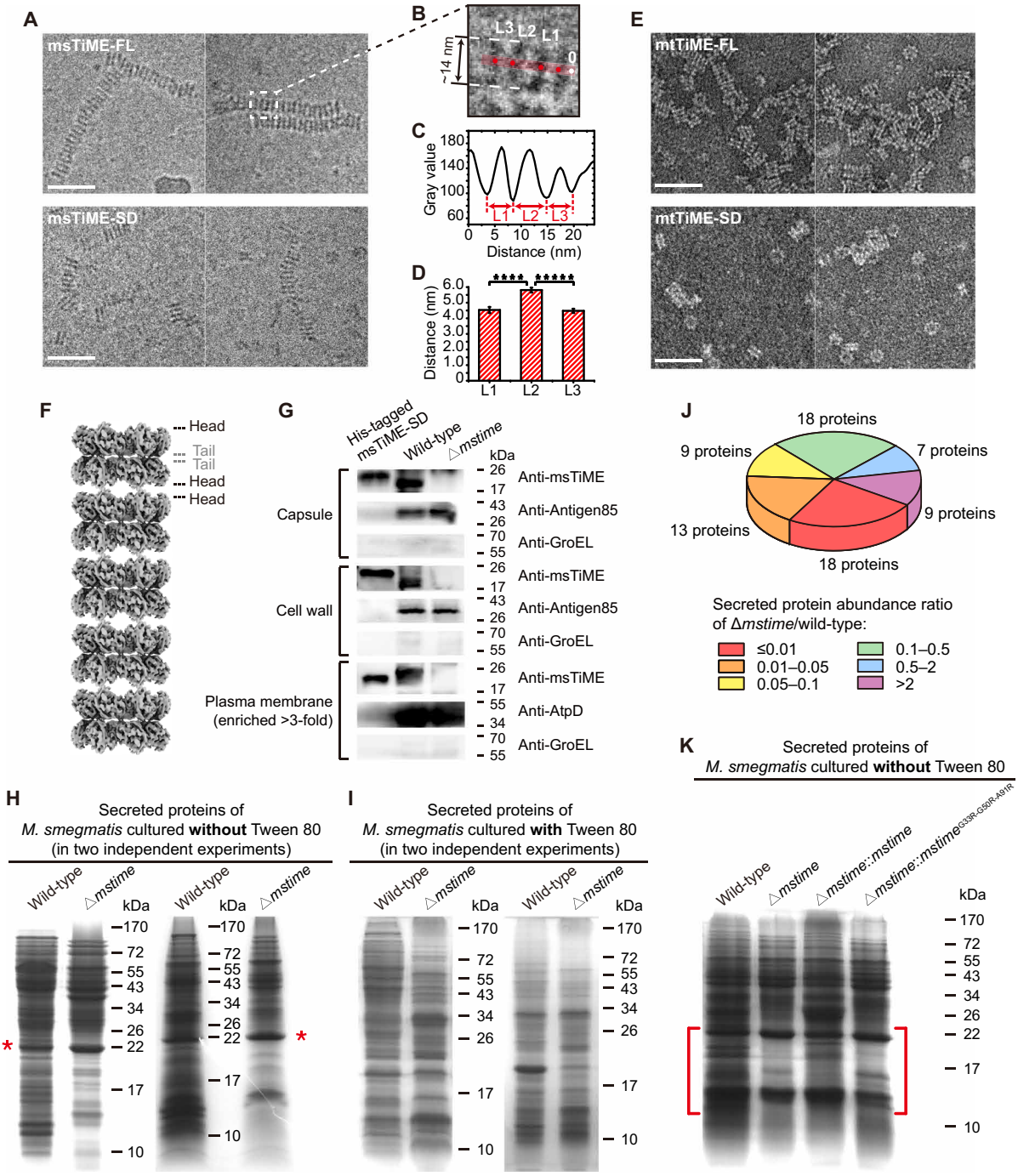

Fig. 3. Double-layered TiME complexes stack into secretion-related tubes. (**A**) Representative cryo-EM images of msTiME-FL (in amphipol) and msTiME-SD. (**B** and **C**) Distances between layers of the enlarged view in (A). (**D**) Intensity range statistics of each layer from selected images. The density profiles were obtained from smoothed images and averaged over a width of 23 pixels by ImageJ. Results are shown as means ± SE ($n = 10$). Two-tailed unpaired t test was used for statistical analysis (****$P < 0.0001$ and *****$P < 0.00001$). (**E**) EM images of negatively stained mtTiME-FL (without amphipol) and mtTiME-SD. Same scale bar corresponding to 50 nm in (A) and (E). (**F**) Tube model of TiME stacked by double-layered complexes. (**G**) msTiME subcellular localization in *M. smegmatis*. Western blot detection of msTiME, Antigen85 (loading control), AtpD (loading control), and GroEL (negative control) from capsule, cell wall, and plasma membrane fractions of wild-type and Δ*mstime* strains. Molecular weight of msTiME detected in the capsule or cell wall was lower than purified His-tagged msTiME-SD overexpressed in *E. coli*; molecular weight of msTiME detected in the plasma membrane was higher than the His-tagged msTiME-SD. (**H** and **I**) SDS-PAGE–based culture medium protein analysis of wild-type and Δ*mstime M. smegmatis* cultured in the medium without (H) or with (I) Tween 80. * indicates a protein band with a molecular weight of ~22 kDa. (**J**) Pie chart distribution of 74 known secreted proteins based on label-free quantitative mass spectrometry. Result is shown from three independent biological replicates. (**K**) SDS-PAGE of culture medium proteins of wild-type, Δ*mstime*, and *mstime*- or *mstime*$^{G33R\text{-}G50R\text{-}A91R}$-complemented strains cultured in the medium without Tween 80. The differences of culture medium protein level between wild-type, Δ*mstime*, and complemented strains are indicated by brackets. Results of (G), (H), (I), and (K) are representative of at least three independent biological replicates.

18 proteins by >100-fold; see Fig. 3J and data S1). Thirty-seven of these 58 secreted proteins have a molecular weight of less than 26 kDa (data S1), consistent with the above SDS-PAGE results (Fig. 3H). In addition, the mRNA level for only 7 of these 58 proteins changed more than twofold (none by more than fivefold) (data S1). Meanwhile, the mRNA level for only 2 of the 56 components we detected for known secretion systems in *M. smegmatis* plasma membrane changed more than twofold (data S2). Together, these results rule out the possibility that the reduction of secreted protein level was caused by transcription down-regulation or differences in their inner membrane secretion systems. Furthermore, the secreted protein level of Δ*mstime* strain was partially restored by expression of *mstime* [Fig. 3K and fig. S9D; the lower expression level of msTiME in the *mstime*-complemented strain compared with that in the wild-type strain might explain the incomplete restoration (fig. S9C)]. However, expression of $mstime^{G33R\text{-}G50R\text{-}A91R}$ mutant that disrupts ring formation (fig. S3, A and C) and $mstime^{N147R\text{-}F148R}$ mutant that disrupts tube formation (fig. S8, F to I) in Δ*mstime* strain both failed to restore the level of secreted proteins (indicated by arrows in fig. S9D) as the expression of *mstime* (fig. S9D). These results indicate that msTiME contributes to *M. smegmatis* protein secretion dependent on its ring-shaped and tubular structure. In addition, wild-type and Δ*mstime M. smegmatis*, cultured in medium containing Tween 80 to disrupt the capsule and surface of the cell wall, did not show a notable difference of protein distribution in medium (Fig. 3I), suggesting that msTiME facilitates protein secretion to cross the outer cell envelope. Therefore, we conclude that TiME tube participates in protein secretion of *M. smegmatis*.

DISCUSSION

Our crystallographic and cryo-EM structures of mtTiME and msTiME show that their oligomerization leads to formation of rotationally symmetric rings. Two layers of rings pack together in a tail-to-tail manner into a ring-shaped complex, which, in turn, stacks together in a head-to-head manner to form tubes (Fig. 3F). Complementary in vivo subcellular localization and secreted protein analyses indicate that msTiME enables proteins to be secreted across *M. smegmatis* outer envelope. It is conceivable that this secretion is actuated by TiME tubes formed across mycobacterial outer envelope. EspC was thought as a probable needle-like secretion channel in *M. tuberculosis* cell envelope (*25*), but no tubular structure or transport function has been demonstrated for EspC. Besides, all of the known mycobacterial secretion apparatuses, including Sec, accessory SecA2, twin-arginine translocation (Tat), and type VII secretion system (T7SS), are located on the plasma membrane (*26*–*28*). The tubular TiME reported here represents the first putative secretion tube across both the cell wall and capsule of mycobacteria.

Among the nine bacterial secretion systems known to date, some have tubular structures (*29*), but stacking D_8 (or D_7) symmetric units to form a tube reported here is unique by comparison (fig. S11). PrgI in T3aSS, flagella FliC in T3bSS, and pilus TraA in T4aSS assemble into helical tubular structures (*29*–*34*). The most similar tube is that formed by Hcp in T6SS injectisome complex. The head-to-tail stacking of C_6 hexametric rings is the native form of Hcp1 tube (*35*–*37*), as are those in native structures of homologous phage tails and pyocin tubes (*38*–*40*). Although in vivo tail-to-tail stacked TiME tubular structures await confirmation, cell envelope localization of msTiME (Fig. 3G) is consistent with this TiME assembly across the outer cell envelope.

The average lengths of TiME-FL and TiME-SD tubes observed in vitro (fig. S8B) are sufficient to transverse mycobacterial cell wall and extend to capsule layer. Nonetheless, this putative secretion tube is more likely formed by TiME-SD. TiME-FL, which is the precursor of TiME-SD, may only temporarily exist in the plasma membrane before its N-terminal signal peptide is cleaved. That is probably why the abundance of msTiME in the plasma membrane is lower than that in the cell wall or capsule of *M. smegmatis* (Fig. 3G). Besides, the msTiME detected in the cell wall or capsule has a lower molecular weight than the one detected in the plasma membrane (Fig. 3G), which also supports that the msTiME protein in the cell wall or capsule is msTiME-SD. Moreover, after msTiME was knocked out, 53 of the above 58 decreased secreted proteins had no obvious decrease in the mRNA level, suggesting that these 53 secreted proteins might be substrates of TiME tube (data S1). Twenty-one of these 53 potential substrates have known structures, and their sizes are all small enough to pass through the 50- to 60-Å pore of TiME-SD (data S1). Nearly all of these 53 proteins were predicted to have a signal peptide recognized by either Sec secretion system, Tat secretion system, or T7SS (data S1). These proteins could be secreted into periplasm through above secretion systems in the plasma membrane. Then, the putative secretion tube of TiME-SD located on mycobacterial cell wall and capsule might transport these proteins from periplasm (fig. S12). Besides, we still cannot rule out the possibility that TiME-FL with pore-forming property (Fig. 2, H to J) works for other function on mycobacterial plasma membrane.

Obviously, these possibilities await clarification and even direct visualization by cryo–electron tomography of live mycobacteria. Nonetheless, our structural and functional analyses support TiME as an enabler in protein secretion in mycobacteria and open the door for structure-based inhibitor design targeting this essential function.

MATERIALS AND METHODS

Reagent

All lipids used in our experiments were obtained from Avanti Polar Lipids. *n*-Decyl-β-D-maltopyranoside (DM), Triton X-100, and amphipol A8-35 were purchased from Anatrace. Bovine serum albumin (BSA), CF, and Tween 80 were obtained from Sigma-Aldrich.

Cloning, protein expression, and purification of Rv3705c and MSMEG_6251 in vitro

The gene encoding full-length Rv3705c [mtTiME, National Center for Biotechnology Information (NCBI) gene ID: 885229; UniProt accession no. I6XI06] was polymerase chain reaction (PCR)–amplified from *M. tuberculosis* H37Rv DNA library. The gene encoding full-length MSMEG_6251 (msTiME, NCBI gene ID: 4530991; UniProt accession no. A0R5N2) was PCR-amplified from *M. smegmatis* mc^2155 DNA library. Mutations of Rv3705c and MSMEG_6251 were introduced using standard PCR-based mutagenesis method and confirmed by DNA sequencing. Detailed information of strains and plasmids about in vitro cloning and protein expression were listed in table S1. All primers used in molecular cloning and mutagenesis were listed in table S2.

Recombinant proteins were expressed in *E. coli* BL21(DE3). Cells were grown in LB broth (table S3) medium with antibiotic (table S1) at 37°C until the OD_{600} (optical density at 600 nm) value reached 0.9 to 1.0 and then induced using 0.2 mM isopropyl-β-D-1-thiogalactopyranoside (Sigma-Aldrich, USA) at 16°C for 20 hours.

The cells were harvested by centrifugation at 3800*g* for 40 min at 4°C (Allegra X-15R, Beckman Coulter, USA) and used immediately.

For purification, the cell pellet was resuspended in lysis buffer (70 mM tris, 300 mM NaCl, pH 8.0) and then lysed with a high-pressure homogenizer (EmulsiFlex-C3, Avestin, Canada) operating at ~18,000 psi. Cell debris was removed by centrifugation at 20,700*g* for 50 min at 4°C (himac CR21GII, HITACHI centrifuge, Japan). The resulting supernatant was ultracentrifuged at 153,720*g* for 90 min at 4°C (Optima L-100XP, Beckman Coulter, USA) to separate soluble fraction and membrane fraction. The soluble fraction was purified using Ni^{2+}–nitrilotriacetic acid (NTA) resin (Qiagen, Valencia, CA, USA) equilibrated with binding buffer (20 mM tris, 200 mM NaCl, pH 8.0) and then further purified by SEC on a Superdex 200 10/300 GL column (GE Healthcare, Piscataway, NJ, USA) equilibrated with SEC buffer I (20 mM tris, 150 mM NaCl, pH 8.0). Besides, membrane fraction was resuspended in binding buffer and solubilized by 1% DM overnight at 4°C by rotating. The proteins extracted from membranes were purified using Ni^{2+}-NTA resin with binding buffer supplemented with 0.2% DM and then further purified by SEC using SEC buffer II [20 mM tris, 150 mM NaCl (pH 8.0), 0.2% DM]. The purified proteins were evaluated by SDS-PAGE. After SEC, the oligomer fraction of proteins was used for the crystallization and EM experiments, and the mixture of monomer and oligomer fractions of proteins was used for the in vitro assays. Mutant proteins were prepared using the same protocol described above.

Crystallization, data collection, and structure determination of Rv3705c-SD and MSMEG_6251-SD

Rv3705c-SD was crystallized in solutions containing 0.2 M lithium sulfate monohydrate, 100 mM tris (pH 8.8), and 15% PEG 3350 (polyethylene glycol, molecular weight 3350) (*41*). MSMEG_6251-SD and Se-Met derivatives were crystallized in solutions containing 0.3 M magnesium formate, 100 mM bis-tris (pH 6.0), and 20% glycerol. Diffraction data were collected on beamline BL17U at the Shanghai Synchrotron Radiation Facility. A total of 180 frames were collected with an oscillation step of 1° and 0.6-s exposure per frame. The crystal-to-detector distance was 400 and 150 mm for Rv3705c-SD and MSMEG_6251-SD, respectively. Diffraction data were processed and scaled using *HKL*-2000 (*42*) and summarized in table S4. The crystal structure of MSMEG_6251-SD was solved initially with Se-Met derivative data by single-wavelength anomalous diffraction method and refined against native crystal diffraction data at 1.5-Å resolution. The structure of Rv3705c-SD was solved by molecular replacement with MSMEG_6251-SD structure as the searching model and refined to 3.3-Å resolution. All of the crystallographic calculation was carried out with CCP4 package (*43*), and the model building and correction were carried out in Coot (*44*). The structure refinement statistics are shown in table S4.

Amphipol-solubilized Rv3705c-FL cryo-EM sample preparation and data collection

DM used in the membrane protein sample purification was exchanged with amphipol A8-35 (*45*) before making EM samples. The purified Rv3705c-FL in DM was mixed with amphipol A8-35 at 1:3 (w/w) at 4°C for 2 hours. Bio-Beads SM-2 Resin (Bio-Rad, CA, USA) was added to the protein sample at a final concentration of 0.25 mg/ml to remove unbounded DM and amphipol A8-35 at 4°C for 13 hours. The sample was then purified through the Superdex 200 10/300 GL SEC column using SEC buffer I.

Sample evaluation and optimization were carried out with negative-stain EM on a Tecnai F20 microscope. Briefly, 3 μl of the amphipol-solubilized Rv3705c-FL sample was applied onto a carbon-coated 300-mesh Cu EM grid and then stained with 2.2% (w/v) uranyl acetate. For cryo-EM, 3 μl of the sample (1 mg/ml) was applied to Quantifoil R2/1 holey grid and plunged into liquid ethane using FEI Vitrobot IV (Thermo Fisher Scientific) after blotting for 3 s at 5°C and 100% relative humidity. The frozen grids were stored in a liquid nitrogen dewar before imaging.

Optimized cryo-EM grids were loaded into a Titan Krios EM operated at 300 kV, equipped with Gatan Quantum imaging filter (GIF) and a post-GIF K2 Summit direct electron detector. Movies were recorded as dose-fractionated frames in super-resolution mode with Leginon (*46*) at a nominal magnification of ×130,000, corresponding to a pixel size of 1.07 Å per pixel (0.535 Å per pixel for super-resolution mode) on the specimen. The GIF slit width was set to 20 eV to remove inelastically scattered electrons. The dose rate on the camera was set to 8.3 electrons/$Å^2$ per second. An exposure time of 12 s was used at a rate of 0.25 s per frame, giving rise to 48 frames and a total dosage of 100 electrons/$Å^2$ for each movie.

Cryo-EM data processing and 3D reconstructions

Dose-fractionated frames in each movie were 2× binned (pixel size, 1.07 Å per pixel) and aligned to generate a dose-weighted micrograph using UCSF Motioncor2 (*47*). The defocus values of micrographs were determined to be in the range of −1.1 and −2.8 μm by CTFFIND4 (*48*). A total of 276,355 particles were picked automatically by RELION 3.0 (*49*) from 1335 micrographs, then extracted in 256 × 256 square pixels, and 2× binned to 128 × 128 square pixels (pixel size, 2.14 Å per pixel) to speed up further data processing. After several rounds of 2D and 3D classifications, 28,290 particles were selected, reextracted in 256 × 256 square pixels, and subjected to auto-refinement by RELION 3.0 with or without D_8 symmetry. A soft mask was used to exclude the flexible region in the center during auto-refinement with D_8 symmetry. The resolutions of the reconstructed cryo-EM maps were estimated to be 4.4 Å (D_8 symmetry) and 6.2 Å (C_1 symmetry) on the basis of the gold-standard Fourier shell correlation (FSC) = 0.143 criterion (*50*). Crystal structures of Rv3705c-SD or MSMEG_6251-SD were rigid body–fitted into the EM density maps by UCSF Chimera (*51*). Visualization of the EM density maps was made by UCSF ChimeraX (*52*), and EM raw images were displayed by ImageJ (*53*).

SEC-MALS analysis

Oligomeric state of Rv3705c-SD was analyzed using SEC-MALS. One hundred microliters of soluble protein sample (20 mg/ml) was loaded onto Superdex 200 10/300 GL column, connected with a Dawn Heleos II light-scattering detector (Wyatt Technology, Santa Barbara, CA, USA) and an Optilab TREX refractive index detector (Wyatt Technology, Santa Barbara, CA, USA). The experiment was performed in the SEC-MALS buffer (0.02% NaN_3, 20 mM tris, and 150 mM NaCl, pH 8.0) at room temperature. The absolute molecular weight was calculated using ASTRA 7 software (Wyatt Technology, Santa Barbara, CA, USA) based on a *dn*/*dc* value of 0.185 ml/g (*dn* is the change in refractive index and *dc* is the change in concentration).

Preparation of unilamellar liposomes

Powders of 1-palmitoyl-2-oleoyl-*sn*-glycero-3-phosphocholine (POPC) and 1-palmitoyl-2-oleoyl-*sn*-glycero-3-phospho-(1′-rac-glycerol)

(POPG) were mixed and well dispersed in chloroform with a molar ratio of 3:1 (POPC: POPG). The solution was gently dried in glass tubes under a stream of N_2 gas and placed under vacuum for 24 hours to further evaporate residual solvent. The lipid film was rehydrated in binding buffer (20 mM tris, 200 mM NaCl, pH 8.0) through about 10 cycles of liquid nitrogen freezing and thawing. To obtain large unilamellar vesicles, liposomes were extruded 21 times through a 100-nm membrane polycarbonate filters (Nucleopore, Pleasanton, CA, USA) using a Mini-Extruder apparatus (Avanti, Alabaster, AL, USA).

Liposome-binding assays

Purified proteins were added into the prepared unilamellar liposome solution to a final molar ratio of 1:500 (protein:lipid). The mixture was rotated at 4°C for 1 hour and dialyzed against binding buffer for 5 days at 4°C using dialysis membrane with a cutoff pore size of 8 kDa. The buffer was changed twice a day. After dialysis, the proteoliposome sample was collected by ultracentrifugation at 160,000*g* for 90 min at 4°C (Optima TLX, Beckman Coulter, USA) and analyzed by 15% SDS-PAGE. NaK channel (tetrameric membrane protein, ~40 kDa) (*54*) and BSA (soluble protein, ~66 kDa) were used as positive and negative controls, respectively.

Single-channel current recording of Rv3705c-FL and MSMEG_6251-FL

Single-channel recordings in planar lipid bilayer were performed using Ionovation Compact (Osnabrück, Germany). The same buffer (5 mM tris, 5 mM Mops, and 150 mM KCl, pH 7.0) was present in both cis- and trans-chambers, which were separated by a 25-μm-thick TEFLON film with an aperture of 120 μm diameter. Voltage was applied across the bilayer using Ag/AgCl electrodes immersed in each chamber. The artificial membrane was formed by painting the solution of POPC/POPG (3:1) in *n*-decane on the aperture, and formation was monitored by capacitance measurement. The proteoliposomes, which reconstituted at a final molar ratio of 1:1200 (protein:lipid), were homogenized by extruding through a 0.4-μm polycarbonate filter using Mini-Extruder apparatus. To insert protein into the planar lipid bilayer, the proteoliposomes (~100 μg/ml) were added to the cis-chamber next to the bilayer after successful formation of a stable bilayer. Fusion of planar lipid bilayer with protein was detected through observation of channel conductance. Currents were measured with a 2-kHz low-pass filter at a 10-kHz sampling rate using an EPC-10 amplifier (HEKA Elektronik, Germany). Data were analyzed using the clampfit software (Axon Instruments, Molecular Devices, San Jose, CA, USA).

Leakage of liposome contents

The prepared dried lipid film was rehydrated with binding buffer to yield a final concentration of 1.7 mg/ml and then dispersed by at least 10 freeze-thaw-sonication cycles until the solution was clear. CF powder was mixed with the liposome solution to a final concentration of 40 mg/ml followed by another 16 freeze-thaw-sonication cycles. After extruding 20 times through a 0.1-μm polycarbonate membrane filter, the CF-loaded liposomes were separated from unencapsulated CF by PD-10 desalting column (GE Healthcare, Piscataway, NJ, USA). The CF-loaded liposomes were diluted to 10 μM and treated with purified TiME octamer proteins in a cuvette at room temperature (membrane proteins in binding buffer with DM; soluble proteins in binding buffer alone). Then, the fluorescence intensity of the released CF was monitored at an excitation wavelength of 492 nm and an emission wavelength of 517 nm using a spectrofluorophotometer (RF-5301PC, SHIMADZU, Japan).

The percentage of leakage was calculated as follows

$$\%\text{Leakage} = [(F - F_{\min})/(F_{\max} - F_{\min})] \times 100$$

$F_{\min}$ was the initial fluorescence intensity of CF-loaded liposomes. $F_{\max}$ was the fluorescence intensity measured after addition of Triton X-100 (final concentration: 0.1%).

Observation of tubular complexes of MSMEG_6251 and Rv3705c by EM

Purified MSMEG_6251-FL protein was reconstituted in amphipol A8-35 as described above and concentrated to 1 mg/ml. Three microliters of the amphipol-solubilized MSMEG_6251-FL was applied to freshly glow-discharged Quantifoil R2/1 holey grid and blotted with FEI Vitrobot IV. Cryo-EM grids of MSMEG_6251-SD were prepared with MSMEG_6251 soluble fraction protein after SEC purification at a concentration of 1 mg/ml. Cryo-EM images were collected with a FEI Tecnai F20 microscope operated at 200 kV.

For tubular Rv3705c-FL EM observation, DM for enwrapping purified Rv3705c-FL was removed by Bio-Beads SM-2 Resin. After removal of detergent, proteins were purified again by SEC on Superdex 200 10/300 GL column using buffer without DM (SEC buffer I). Rv3705c-FL (0.1 mg/ml) without any detergent or lipid was applied to negative-stain sample preparation. Images were collected with a FEI Tecnai F20 microscope operated at 200 kV.

Negative-stain EM grids of Rv3705c-SD were prepared with Rv3705c soluble fraction protein after SEC purification at a concentration of 0.05 mg/ml. Images were collected with a FEI Tecnai T12 microscope operated at 120 kV.

Negative-stain EM grids of Rv3705c-SD$^{D145R\text{-}G146R}$ and MSMEG_6251-SD$^{N147R\text{-}F148R}$ were prepared with Rv3705c$^{D145R\text{-}G146R}$ and MSMEG_6251$^{N147R\text{-}F148R}$ soluble fraction proteins after SEC purification at a concentration of 0.05 mg/ml. Images were collected with a FEI Tecnai F20 microscope operated at 200 kV.

Construction of *msmeg_6251* knockout strain

M. smegmatis mc^{2}155 *msmeg_6251* knockout strain was constructed by allelic recombination. Plasmids pJV53–green fluorescent protein (GFP) and PUC-Hyg (provided by Y.-C. Sun, MOH Key Laboratory of Systems Biology of Pathogens, Institute of Pathogen Biology, and Center for Tuberculosis Research, Chinese Academy of Medical Sciences and Peking Union Medical College, Beijing, P.R. China) were used for deletion of *M. smegmatis msmeg_6251* gene (*55*). Related plasmid and primer information in this knockout assay was listed in tables S1 and S2, respectively.

A 540–base pair (bp) DNA fragment upstream of *msmeg_6251* (P1) and a 569-bp DNA fragment downstream of *msmeg_6251* (P2) were amplified by PCR and cloned into the PUC-Hyg vector to generate an integrating PUC-Hyg-P1-P2 plasmid (fig. S9A). pJV53-GFP plasmid was electrotransformed into *M. smegmatis* mc^{2}155 to prepare competent *M. smegmatis* containing gp60 and gp61 proteins of mycobacteriophage Che9c as previously reported (*55*, *56*). The competent cells were electrotransformed with PUC-Hyg-P1-P2 plasmid to recombine with *msmeg_6251* gene (fig. S9A). Transformants were incubated at 37°C for 4 hours to recover and plated on Middlebrook 7H10 agar (BD Difco) medium supplemented with 0.2% glycerol, 0.02% tyloxapol, kanamycin, and hygromycin (table S1).

Bacteria were cultured for 3 days at 37°C, colonies were picked to verify by PCR, and then the recombined colonies were further cultured. The final strains were grown in the 7H10 agar medium with 10% sucrose to eliminate pJV53-GFP. GFP-negative colonies (loss of pJV53-GFP) were picked up for PCR (fig. S9B), and PCR products were sequenced to confirm the excision of the *dif*-antibiotic cassette. Additional Western blot (fig. S9C) confirmed that MSMEG_6251 was not expressed in *msmeg_6251* knockout strain.

MSMEG_6251 subcellular localization

Different fractions of *M. smegmatis* mc^2155 envelope, including capsule, cell wall, and plasma membrane, were extracted separately to identify the subcellular localization of MSMEG_6251. To extract the capsule fraction, wild-type *M. smegmatis* mc^2155 were grown in 7H9 broth (BD Difco) B medium (table S3) at 37°C for 2 days to exponential phase and then harvested by centrifugation at 3000*g* for 15 min at 4°C. Bacteria were washed softly three times with phosphate-buffered saline (PBS) buffer (1.47 mM KH_2PO_4, 8.1 mM Na_2HPO_4, 2.67 mM KCl, and 138 mM NaCl, pH 7.4) by centrifugation and resuspended in the same buffer. Bacteria were incubated with PBS buffer containing 1% Tween 80 for 30 min at room temperature before centrifugation to separate capsule fraction from bacterial cells. The resulting supernatant was filtrated with a 0.22-μm pore size filter to remove residual cells. For analysis of protein content, the extracted proteins in capsule fraction were concentrated by trichloroacetic acid (TCA) precipitation (*5*, *57*).

To extract the cell wall and plasma membrane fractions, wild-type *M. smegmatis* mc^2155 were grown in 7H9 broth A medium (table S3) at 37°C for 2 days and then were harvested at the same condition as mentioned above. Pellet of 200 ml of bacteria was washed once with PBS buffer containing 1 mM EDTA and resuspended in the same buffer for extracting cell wall. The same operation was applied to pellet of 600 ml of bacteria for plasma membrane extraction by high-salt buffer [2 M NaCl, 10 mM Hepes-NaOH (pH 7.4), 1 mM EDTA]. Bacteria were lysed with a high-pressure homogenizer (EmulsiFlex-C3, Avestin, Canada) operating at ~22,000 psi for 20 min. Unbroken bacteria were removed by centrifugation twice at 3000*g* for 10 min. Bacterial lysate was centrifugated at 10,000*g* for 40 min to yield crude cell wall fraction (pellet P1). The supernatant was centrifuged at 27,000*g* for 30 min to remove residual cell wall pellet, and then crude plasma membrane (pellet P2) was collected from the resulting supernatant through ultracentrifugation at 100,000*g* for 1 hour. Pellet P1 was washed slightly for three times with PBS buffer containing 1 mM EDTA and resuspended in the same buffer, and pellet P2 was also treated in this way by high-salt buffer. Then, pellets P1 and P2 were layered on a sucrose step gradient in Ultra-Clear ultracentrifuge tubes (part no. 344058, Beckman Coulter, USA), respectively. The discontinuous sucrose gradient consisted of 10% [1 Vol] – 20% [1 Vol] – 30% [3 Vol] – 36% [3 Vol] – 40% [1 Vol] – 50% [1 Vol] – 60% [1 Vol] to separate two membrane fractions of *M. smegmatis*. The gradients were ultracentrifuged at 100,000*g* for at least 2 hours before collecting cell wall and plasma membrane fractions from sucrose gradients by puncture. The plasma membrane fraction was further resuspended with 10-fold volume carbonate buffer (0.1 M Na_2CO_3, 1 mM EDTA, pH 11.3) and ultracentrifuged at 100,000*g* for 1 hour. The pellet was homogenized and incubated for 30 min in the carbonate buffer and then ultracentrifuged at 100,000*g* for 1 hour, and this step was followed by resuspending with wash buffer [4 M urea, 100 mM NaCl, 10 mM Hepes-NaOH (pH 7.4), 1 mM EDTA]. After ultracentrifugation at 100,000*g* for 1 hour, the final plasma membrane fraction pellet was resuspended in dissolution buffer [0.25 M sucrose, 100 mM NaCl, 10 mM Hepes-NaOH (pH 7.4), 1 mM EDTA, and 1% SDS]. All steps above were operated at 4°C (*16*, *58*–*61*).

For Western blot, the following primary antibodies were used: polyclonal anti-msTiME antibody (rabbit), which was generated by immunization of rabbits with the purified His-tagged MSMEG_6251-SD fusion protein, in collaboration with the Institute of Genetics and Development, Chinese Academy of Sciences (1:2500 dilution); monoclonal anti-Antigen85 (mouse) from Santa Cruz Biotechnology (sc-57611; 1:200 dilution); monoclonal anti–adenosine triphosphate (ATP) synthase β (AtpD) (mouse) from Invitrogen (A-21351; 1:500 dilution); and polyclonal anti-GroEL (rabbit) from Abcam (ab90522; 1:1000 dilution). Secondary antibodies used were horseradish peroxidase (HRP)–conjugated goat anti-rabbit immunoglobulin G (IgG) antibody from Promega (W401B; 1:2500 dilution) and HRP-conjugated goat anti-mouse IgG antibody from Abcam (ab6789; 1:1000 dilution). Purified msTiME-SD with C-terminal LEHHHHHH tag overexpressed in *E. coli* was used as positive control. Antigen85 was used as an internal control for the capsule and cell wall fractions, AtpD was used as an internal control for the plasma membrane fraction, and GroEL was used as the negative control.

Complementation of *msmeg_6251* knockout strain

The *E. coli*/mycobacterial shuttle vector pMV361D was used as the complementation vector for the expression of MSMEG_6251, $MSMEG\_6251^{G33R\text{-}G50R\text{-}A91R}$, or $MSMEG\_6251^{N147R\text{-}F148R}$ in *msmeg_6251* knockout *M. smegmatis*. The pMV361D plasmid was derived from the pMV361 plasmid (*62*) by deleting ATG bases at the *hsp60* sequence start site, in which its sequence was used to promote expression of the foreign antigen gene (*62*). Consequently, there is no extra residue in front of the N-terminal signal peptide of MSMEG_6251. The genes of *msmeg_6251*, $msmeg\_6251^{G33R\text{-}G50R\text{-}A91R}$, or $msmeg\_6251^{N147R\text{-}F148R}$ were cloned into the pMV361D vector. Then, these recombinant plasmids were electrotransformed into *msmeg_6251* knockout *M. smegmatis*. Related plasmid and primer information in this assay was listed in tables S1 and S2, respectively. The expression of MSMEG_6251, $MSMEG\_6251^{G33R\text{-}G50R\text{-}A91R}$, or $MSMEG\_6251^{N147R\text{-}F148R}$ was confirmed by Western blot analysis (fig. S9C).

SDS-PAGE and label-free mass spectrometry protein quantification of the *M. smegmatis* secreted proteins

To compare the secreted proteins of the *M. smegmatis* mc^2155 wild-type and *msmeg_6251* knockout strains, we used SDS-PAGE and label-free mass spectrometry protein quantification analyses. *M. smegmatis* stains were grown to OD_{600} 0.2 to 0.3 in 600-ml 7H9 broth A or B medium at 37°C. The culture medium was centrifuged at 3000*g* for 30 min at 4°C to remove the bacteria, and the supernatant was filtered through a 0.45-μm membrane followed by a 0.22-μm membrane. The resulting filtrate was treated with precooled TCA to a final concentration of 10% (v/v), the mixture was incubated on ice for 1 hour, and the precipitate was obtained after 36,800*g* for 15 min at 4°C. The precipitate was washed by 40 ml of pre-cold acetone three times. The supernatant was discarded very carefully, and the washed protein pellet was air-dried and weighed. Each strain was prepared in triplicate. The weight of protein pellet in each independent biological replicate was kept equivalent.

Secreted protein samples for SDS-PAGE were prepared from the bacteria cultured in 7H9 broth A or B medium. Appropriate protein pellet was resuspended in 2× loading buffer prepared for SDS-PAGE.

Secreted protein samples for mass spectrometry were prepared from the bacteria cultured in 7H9 broth B. Mass spectrometry protein quantification analysis was supported by J. Wang (Laboratory of Proteomics, Institute of Biophysics, Chinese Academy of Sciences, Beijing, P.R. China). The nanoliquid chromatography–tandem mass spectrometry experiments were performed on a Q Exactive (Thermo Fisher Scientific, USA) equipped with an Easy n-LC 1000 high-performance liquid chromatography system (Thermo Fisher Scientific, USA). The raw data from Q Exactive were analyzed with Proteome Discovery 2.2.0.388 using Sequest HT search engine for protein identification and Percolator for false discovery rate analysis. The UniProt *M. smegmatis* protein database (updated on March 2019) was used for searching the data. Protein label-free quantification was also performed on Proteome Discovery 2.2.0.388 using the areas of identified peptides. Only unique and razor peptides of proteins were selected for protein relative quantification. The normalization to the peptide median of each sample was used to correct experimental bias, and the total peptide amount was selected in normalization mode. The protein abundance ratio value of culture filtrate protein from *msmeg_6251* knockout and wild-type strains was represented by median of peptide abundance ratios of all possible pairwise peptides; these protein abundance ratios can be used to identify whether proteins were secreted differentially between two strains.

Transcriptome sequencing

M. smegmatis mc^2155 wild-type and *msmeg_6251* knockout strains were cultured in 7H9 broth A medium at 37°C. When OD_{600} values reached 1.0, bacteria were collected and washed three times with PBS buffer for RNA sequencing (RNA-seq). Each strain was prepared in triplicate. RNA-seq uses the capabilities of high-throughput sequencing methods to provide insight into the transcriptome of *M. smegmatis*. The transcriptome of *M. smegmatis* was sequenced and analyzed by Sangon Biotech (Shanghai) Co. Ltd. (P.R. China). Differential expression analysis of two samples was performed using DESeq2. TopGO was used for GO (gene ontology) enrichment analysis. ClusterProfiler was used for the classification and enrichment analysis of KEGG (Kyoto Encyclopedia of Genes and Genomes) pathway and COG (Clusters of Orthologous Groups).

SUPPLEMENTARY MATERIALS

Supplementary material for this article is available at http://advances.sciencemag.org/cgi/content/full/7/34/eabg5656/DC1

View/request a protocol for this paper from *Bio-protocol*.

REFERENCES AND NOTES

1. I. Barberis, N. L. Bragazzi, L. Galluzzo, M. Martini, The history of tuberculosis: From the first historical records to the isolation of Koch's bacillus. *J. Prev. Med. Hyg.* **58**, E9–E12 (2017).
2. W. Kingston, Streptomycin, *Schatz v. Waksman*, and the balance of credit for discovery. *J. Hist. Med. Allied Sci.* **59**, 441–462 (2004).
3. N. R. Gandhi, P. Nunn, K. Dheda, H. S. Schaaf, M. Zignol, D. van Soolingen, P. Jensen, J. Bayona, Multidrug-resistant and extensively drug-resistant tuberculosis: A threat to global control of tuberculosis. *Lancet* **375**, 1830–1843 (2010).
4. M. M. Braun, T. R. Coté, C. S. Rabkin, Trends in death with tuberculosis during the AIDS era. *JAMA* **269**, 2865–2868 (1993).
5. M. Sani, E. N. G. Houben, J. Geurtsen, J. Pierson, K. de Punder, M. van Zon, B. Wever, S. R. Piersma, C. R. Jiménez, M. Daffé, B. J. Appelmelk, W. Bitter, N. van der Wel, P. J. Peters, Direct visualization by cryo-EM of the mycobacterial capsular layer: A labile structure containing ESX-1-secreted proteins. *PLOS Pathog.* **6**, e1000794 (2010).
6. P. J. Brennan, H. Nikaido, The envelope of mycobacteria. *Annu. Rev. Biochem.* **64**, 29–63 (1995).
7. M. Daffe, P. Draper, The envelope layers of mycobacteria with reference to their pathogenicity. *Adv. Microb. Physiol.* **39**, 131–203 (1998).
8. D. E. Minnikin, O. Y. Lee, H. H. Wu, V. Nataraj, H. D. Donoghue, M. Ridell, M. Watanabe, L. Alderwick, A. Bhatt, G. S. Besra, Pathophysiological implications of cell envelope structure in *Mycobacterium tuberculosis* and related taxa, in *Tuberculosis: Expanding Knowledge*, W. Ribón, Ed. (InTech Open Access Publisher, 2015), pp. 145–175.
9. M. A. Forrellad, L. I. Klepp, A. Gioffré, J. Sabio y García, H. R. Morbidoni, M. de la Paz Santangelo, A. A. Cataldi, F. Bigi, Virulence factors of the *Mycobacterium tuberculosis* complex. *Virulence* **4**, 3–66 (2013).
10. P. S. Renshaw, K. L. Lightbody, V. Veverka, F. W. Muskett, G. Kelly, T. A. Frenkiel, S. V. Gordon, R. G. Hewinson, B. Burke, J. Norman, R. A. Williamson, M. D. Carr, Structure and function of the complex formed by the tuberculosis virulence factors CFP-10 and ESAT-6. *EMBO J.* **24**, 2491–2498 (2005).
11. R. Singh, S. P. Dwivedi, U. S. Gaharwar, R. Meena, P. Rajamani, T. Prasad, Recent updates on drug resistance in *Mycobacterium tuberculosis*. *J. Appl. Microbiol.* **128**, 1547–1567 (2020).
12. D. C. Rodríguez, M. Ocampo, C. Reyes, G. Arévalo-Pinzón, M. Munoz, M. A. Patarroyo, M. E. Patarroyo, Cell-peptide specific interaction can inhibit *Mycobacterium tuberculosis H37Rv* infection. *J. Cell. Biochem.* **117**, 946–958 (2016).
13. T. Melak, S. Gakkhar, Potential non homologous protein targets of mycobacterium tuberculosis H37Rv identified from protein-protein interaction network. *J. Theor. Biol.* **361**, 152–158 (2014).
14. H. Målen, F. S. Berven, K. E. Fladmark, H. G. Wiker, Comprehensive analysis of exported proteins from *Mycobacterium tuberculosis* H37Rv. *Proteomics* **7**, 1702–1718 (2007).
15. J. Kyte, R. F. Doolittle, A simple method for displaying the hydropathic character of a protein. *J. Mol. Biol.* **157**, 105–132 (1982).
16. L. Chiaradia, C. Lefebvre, J. Parra, J. Marcoux, O. Burlet-Schiltz, G. Etienne, M. Tropis, M. Daffé, Dissecting the mycobacterial cell envelope and defining the composition of the native mycomembrane. *Sci. Rep.* **7**, 12807 (2017).
17. A. M. Abdallah, T. Verboom, E. M. Weerdenburg, N. C. Gey van Pittius, P. W. Mahasha, C. Jiménez, M. Parra, N. Cadieux, M. J. Brennan, B. J. Appelmelk, W. Bitter, PPE and PE_PGRS proteins of *Mycobacterium marinum* are transported via the type VII secretion system ESX-5. *Mol. Microbiol.* **73**, 329–340 (2009).
18. M. H. Daleke, R. Ummels, P. Bawono, J. Heringa, C. M. J. E. Vandenbroucke-Grauls, J. Luirink, W. Bitter, General secretion signal for the mycobacterial type VII secretion pathway. *Proc. Natl. Acad. Sci. U.S.A.* **109**, 11342–11347 (2012).
19. C. Bell, G. T. Smith, M. J. Sweredoski, S. Hess, Characterization of the *Mycobacterium tuberculosis* proteome by liquid chromatography mass spectrometry-based proteomics techniques: A comprehensive resource for tuberculosis research. *J. Proteome Res.* **11**, 119–130 (2012).
20. C. Mehaffy, A. Hess, J. E. Prenni, B. Mathema, B. Kreiswirth, K. M. Dobos, Descriptive proteomic analysis shows protein variability between closely related clinical isolates of *Mycobacterium tuberculosis*. *Proteomics* **10**, 1966–1984 (2010).
21. E. F. Perkowski, K. E. Zulauf, D. Weerakoon, J. D. Hayden, T. R. Ioerger, D. Oreper, S. M. Gomez, J. C. Sacchettini, M. Braunstein, The EXIT strategy: An approach for identifying bacterial proteins exported during host infection. *MBio* **8**, e00333-17 (2017).
22. A. Tschumi, T. Grau, D. Albrecht, M. Rezwan, H. Antelmann, P. Sander, Functional analyses of mycobacterial lipoprotein diacylglyceryl transferase and comparative secretome analysis of a mycobacterial *lgt* mutant. *J. Bacteriol.* **194**, 3938–3949 (2012).
23. M. H. Touchette, E. R. Van Vlack, L. Bai, J. Kim, A. B. Cognetta III, M. L. Previti, K. M. Backus, D. W. Martin, B. F. Cravatt, J. C. Seeliger, A screen for protein-protein interactions in live mycobacteria reveals a functional link between the virulence-associated lipid transporter LprG and the mycolyltransferase antigen 85A. *ACS Infect. Dis.* **3**, 336–348 (2017).
24. G. A. de Souza, M. Ø. Arntzen, S. Fortuin, A. C. Schürch, H. Målen, C. R. E. McEvoy, D. van Soolingen, B. Thiede, R. M. Warren, H. G. Wiker, Proteogenomic analysis of polymorphisms and gene annotation divergences in prokaryotes using a clustered mass spectrometry-friendly database. *Mol. Cell. Proteomics* **10**, M110.002527 (2011).
25. Y. Lou, J. Rybniker, C. Sala, S. T. Cole, EspC forms a filamentous structure in the cell envelope of *Mycobacterium tuberculosis* and impacts ESX-1 secretion. *Mol. Microbiol.* **103**, 26–38 (2017).
26. L. S. Ligon, J. D. Hayden, M. Braunstein, The ins and outs of *Mycobacterium tuberculosis* protein export. *Tuberculosis (Edinb.)* **92**, 121–132 (2012).
27. M. E. Feltcher, J. T. Sullivan, M. Braunstein, Protein export systems of *Mycobacterium tuberculosis*: Novel targets for drug development? *Future Microbiol.* **5**, 1581–1597 (2010).
28. M. I. Gröschel, F. Sayes, R. Simeone, L. Majlessi, R. Brosch, ESX secretion systems: Mycobacterial evolution to counter host immunity. *Nat. Rev. Microbiol.* **14**, 677–691 (2016).

29. C. Rapisarda, M. Tassinari, F. Gubellini, R. Fronzes, Using cryo-EM to investigate bacterial secretion systems. *Annu. Rev. Microbiol.* **72**, 231–254 (2018).
30. M. Desvaux, M. Hébraud, I. R. Henderson, M. J. Pallen, Type III secretion: What's in a name? *Trends Microbiol.* **14**, 157–160 (2006).
31. A. Loquet, N. G. Sgourakis, R. Gupta, K. Giller, D. Riedel, C. Goosmann, C. Griesinger, M. Kolbe, D. Baker, S. Becker, A. Lange, Atomic model of the type III secretion system needle. *Nature* **486**, 276–279 (2012).
32. F. Wang, A. M. Burrage, S. Postel, R. E. Clark, A. Orlova, E. J. Sundberg, D. B. Kearns, E. H. Egelman, A structural model of flagellar filament switching across multiple bacterial species. *Nat. Commun.* **8**, 960 (2017).
33. T. R. D. Costa, A. Ilangovan, M. Ukleja, A. Redzej, J. M. Santini, T. K. Smith, E. H. Egelman, G. Waksman, Structure of the bacterial sex F pilus reveals an assembly of a stoichiometric protein-phospholipid complex. *Cell* **166**, 1436–1444.e10 (2016).
34. K. Wallden, A. Rivera-Calzada, G. Waksman, Type IV secretion systems: Versatility and diversity in function. *Cell. Microbiol.* **12**, 1203–1212 (2010).
35. J. D. Mougous, M. E. Cuff, S. Raunser, A. Shen, M. Zhou, C. A. Gifford, A. L. Goodman, G. Joachimiak, C. L. Ordoñez, S. Lory, T. Walz, A. Joachimiak, J. J. Mekalanos, A virulence locus of *Pseudomonas aeruginosa* encodes a protein secretion apparatus. *Science* **312**, 1526–1530 (2006).
36. E. R. Ballister, A. H. Lai, R. N. Zuckermann, Y. Cheng, J. D. Mougous, *In vitro* self-assembly of tailorable nanotubes from a simple protein building block. *Proc. Natl. Acad. Sci. U.S.A.* **105**, 3733–3738 (2008).
37. D. L. Clemens, P. Ge, B.-Y. Lee, M. A. Horwitz, Z. H. Zhou, Atomic structure of T6SS reveals interlaced array essential to function. *Cell* **160**, 940–951 (2015).
38. N. M. I. Taylor, N. S. Prokhorov, R. C. Guerrero-Ferreira, M. M. Shneider, C. Browning, K. N. Goldie, H. Stahlberg, P. G. Leiman, Structure of the T4 baseplate and its function in triggering sheath contraction. *Nature* **533**, 346–352 (2016).
39. P. Ge, D. Scholl, P. G. Leiman, X. Yu, J. F. Miller, Z. H. Zhou, Atomic structures of a bactericidal contractile nanotube in its pre- and postcontraction states. *Nat. Struct. Mol. Biol.* **22**, 377–382 (2015).
40. P. Ge, D. Scholl, N. S. Prokhorov, J. Avaylon, M. M. Shneider, C. Browning, S. A. Buth, M. Plattner, U. Chakraborty, K. Ding, P. G. Leiman, J. F. Miller, Z. H. Zhou, Action of a minimal contractile bactericidal nanomachine. *Nature* **580**, 658–662 (2020).
41. F. Lu, F. Gao, H. Li, W. Gong, L. Zhou, L. Bi, Purification, crystallization and preliminary X-ray crystallographic studies of Rv3705c from *Mycobacterium tuberculosis*. *Acta Crystallogr. F Struct. Biol. Commun.* **70**, 1090–1092 (2014).
42. Z. Otwinowski, W. Minor, Processing of X-ray diffraction data collected in oscillation mode. *Methods Enzymol.* **276**, 307–326 (1997).
43. M. D. Winn, C. C. Ballard, K. D. Cowtan, E. J. Dodson, P. Emsley, P. R. Evans, R. M. Keegan, E. B. Krissinel, A. G. W. Leslie, A. McCoy, S. J. McNicholas, G. N. Murshudov, N. S. Pannu, E. A. Potterton, H. R. Powell, R. J. Read, A. Vagin, K. S. Wilson, Overview of the *CCP4* suite and current developments. *Acta Crystallogr. D Biol. Crystallogr.* **67**, 235–242 (2011).
44. P. Emsley, B. Lohkamp, W. G. Scott, K. Cowtan, Features and development of Coot. *Acta Crystallogr. D Biol. Crystallogr.* **66**, 486–501 (2010).
45. M. Flötenmeyer, H. Weiss, C. Tribet, J.-L. Popot, K. Leonard, The use of amphipathic polymers for cryo electron microscopy of NADH:ubiquinone oxidoreductase (complex I). *J. Microsc.* **227**, 229–235 (2007).
46. C. Suloway, J. Pulokas, D. Fellmann, A. Cheng, F. Guerra, J. Quispe, S. Stagg, C. S. Potter, B. Carragher, Automated molecular microscopy: The new Leginon system. *J. Struct. Biol.* **151**, 41–60 (2005).
47. S. Q. Zheng, E. Palovcak, J.-P. Armache, K. A. Verba, Y. Cheng, D. A. Agard, MotionCor2: Anisotropic correction of beam-induced motion for improved cryo-electron microscopy. *Nat. Methods* **14**, 331–332 (2017).
48. A. Rohou, N. Grigorieff, CTFFIND4: Fast and accurate defocus estimation from electron micrographs. *J. Struct. Biol.* **192**, 216–221 (2015).
49. S. H. W. Scheres, RELION: Implementation of a Bayesian approach to cryo-EM structure determination. *J. Struct. Biol.* **180**, 519–530 (2012).
50. P. B. Rosenthal, R. Henderson, Optimal determination of particle orientation, absolute hand, and contrast loss in single-particle electron cryomicroscopy. *J. Mol. Biol.* **333**, 721–745 (2003).
51. E. F. Pettersen, T. D. Goddard, C. C. Huang, G. S. Couch, D. M. Greenblatt, E. C. Meng, T. E. Ferrin, UCSF Chimera––A visualization system for exploratory research and analysis. *J. Comput. Chem.* **25**, 1605–1612 (2004).
52. T. D. Goddard, C. C. Huang, E. C. Meng, E. F. Pettersen, G. S. Couch, J. H. Morris, T. E. Ferrin, UCSF ChimeraX: Meeting modern challenges in visualization and analysis. *Protein Sci.* **27**, 14–25 (2018).
53. C. A. Schneider, W. S. Rasband, K. W. Eliceiri, NIH Image to ImageJ: 25 years of image analysis. *Nat. Methods* **9**, 671–675 (2012).
54. C. Shi, Y. He, K. Hendriks, B. L. de Groot, X. Cai, C. Tian, A. Lange, H. Sun, A single NaK channel conformation is not enough for non-selective ion conduction. *Nat. Commun.* **9**, 717 (2018).
55. X.-J. Mao, M.-Y. Yan, H. Zhu, X.-P. Guo, Y.-C. Sun, Efficient and simple generation of multiple unmarked gene deletions in *Mycobacterium smegmatis*. *Sci. Rep.* **6**, 22922 (2016).
56. A. Cascioferro, F. Boldrin, A. Serafini, R. Provvedi, G. Palù, R. Manganelli, Xer site-specific recombination, an efficient tool to introduce unmarked deletions into mycobacteria. *Appl. Environ. Microbiol.* **76**, 5312–5316 (2010).
57. F. Carlsson, S. A. Joshi, L. Rangell, E. J. Brown, Polar localization of virulence-related Esx-1 secretion in mycobacteria. *PLOS Pathog.* **5**, e1000285 (2009).
58. C. H. Marchand, C. Salmeron, R. B. Raad, X. Méniche, M. Chami, M. Masi, D. Blanot, M. Daffé, M. Tropis, E. Huc, P. Le Maréchal, P. Decottignies, N. Bayan, Biochemical disclosure of the mycolate outer membrane of *Corynebacterium glutamicum*. *J. Bacteriol.* **194**, 587–597 (2012).
59. A. Ortalo-Magné, M.-A. Dupont, A. Lemassu, A. B. Andersen, P. Gounon, M. Daffé, Molecular composition of the outermost capsular material of the tubercle bacillus. *Microbiology* **141**, 1609–1620 (1995).
60. J. V. Olsen, P. A. Nielsen, J. R. Andersen, M. Mann, J. R. Wiśniewski, Quantitative proteomic profiling of membrane proteins from the mouse brain cortex, hippocampus, and cerebellum using the HysTag reagent: Mapping of neurotransmitter receptors and ion channels. *Brain Res.* **1134**, 95–106 (2007).
61. R. J. Wiśniewski, Protocol to enrich and analyze plasma membrane proteins. *Methods Mol. Biol.* **528**, 127–134 (2009).
62. C. K. Stover, V. F. de la Cruz, T. R. Fuerst, J. E. Burlein, L. A. Benson, L. T. Bennett, G. P. Bansal, J. F. Young, M. H. Lee, G. F. Hatfull, S. B. Snapper, R. G. Barletta, W. R. Jacobs Jr., B. R. Bloom, New use of BCG for recombinant vaccines. *Nature* **351**, 456–460 (1991).
63. X.-Y. Pei, P. Hinchliffe, M. F. Symmons, E. Koronakis, R. Benz, C. Hughes, V. Koronakis, Structures of sequential open states in a symmetrical opening transition of the TolC exit duct. *Proc. Natl. Acad. Sci. U.S.A.* **108**, 2112–2117 (2011).
64. Y. Gu, Y. Zeng, Z. Wang, C. Dong, BamA β16C strand and periplasmic turns are critical for outer membrane protein insertion and assembly. *Biochem. J.* **474**, 3951–3961 (2017).
65. P. Goyal, P. V. Krasteva, N. Van Gerven, F. Gubellini, I. Van den Broeck, A. Troupiotis-Tsaïlaki, W. Jonckheere, G. Péhau-Arnaudet, J. S. Pinkner, M. R. Chapman, S. J. Hultgren, S. Howorka, R. Fronzes, H. Remaut, Structural and mechanistic insights into the bacterial amyloid secretion channel CsgG. *Nature* **516**, 250–253 (2014).
66. Z. Yan, M. Yin, D. Xu, Y. Zhu, X. Li, Structural insights into the secretin translocation channel in the type II secretion system. *Nat. Struct. Mol. Biol.* **24**, 177–183 (2017).
67. L. J. Worrall, C. Hong, M. Vuckovic, W. Deng, J. R. C. Bergeron, D. D. Majewski, R. K. Huang, T. Spreter, B. B. Finlay, Z. Yu, N. C. J. Strynadka, Near-atomic-resolution cryo-EM analysis of the *Salmonella* T3S injectisome basal body. *Nature* **540**, 597–601 (2016).
68. G. G. Sgro, T. R. D. Costa, W. Cenens, D. P. Souza, A. Cassago, L. Coutinho de Oliveira, R. K. Salinas, R. V. Portugal, C. S. Farah, G. Waksman, Cryo-EM structure of the bacteria-killing type IV secretion system core complex from *Xanthomonas citri*. *Nat. Microbiol.* **3**, 1429–1440 (2018).
69. J. Hu, L. J. Worrall, M. Vuckovic, C. Hong, W. Deng, C. E. Atkinson, B. Brett Finlay, Z. Yu, N. C. J. Strynadka, T3S injectisome needle complex structures in four distinct states reveal the basis of membrane coupling and assembly. *Nat. Microbiol.* **4**, 2010–2019 (2019).
70. N. Noinaj, A. J. Kuszak, C. Balusek, J. C. Gumbart, S. K. Buchanan, Lateral opening and exit pore formation are required for BamA function. *Structure* **22**, 1055–1062 (2014).
71. C. L. Dulberger, E. J. Rubin, C. C. Boutte, The mycobacterial cell envelope – A moving target. *Nat. Rev. Microbiol.* **18**, 47–59 (2020).
72. A. Mohan, J. Padiadpu, P. Baloni, N. Chandra, Complete genome sequences of a *Mycobacterium smegmatis* laboratory strain (MC^2 155) and isoniazid-resistant (4XR1/R2) mutant strains. *Genome Announc.* **3**, e01520-14 (2015).

Acknowledgments: We thank the team of beamline BL17U in Shanghai Synchrotron Radiation Facility for diffraction data collection. The pJV53-GFP and PUC-Hyg plasmids were provided by Y.-C. Sun (MOH Key Laboratory of Systems Biology of Pathogens, Institute of Pathogen Biology, Chinese Academy of Medical Sciences and Peking Union Medical College, Beijing, P.R. China). Mass spectrometry technology was supported by J. Wang (Laboratory of Proteomics, Institute of Biophysics, Chinese Academy of Sciences, Beijing 100101, P.R. China). **Funding:** This research has been supported, in part, by the National Natural Science Foundation of China (grants 31570841 and U1732264 to W.G.), the National Key R&D Program of China (grant 2017YFA0504900 to W.G.), and the U.S. NIH (GM071940, DE028583, DE025567, and AI094386 to Z.H.Z.). We acknowledge the use of resources at the Electron Imaging Center for Nanomachines supported by UCLA and by instrumentation grants from NIH (1S10RR23057 and 1U24GM116792) and NSF (DBI-1338135 and DMR-1548924). **Author contributions:** W.G., Z.H.Z., and L.B. conceived the project. W.G. and Z.H.Z. supervised the research. X.C. and L.L. carried out cloning and protein preparation, and W.G. determined the crystal structures. X.C. and C.Q. prepared cryo-EM sample. C.Q., S.L., and X.Z. performed negative-stain imaging. Y.C. and C.Q. collected cryo-EM data, and Y.H. and C.Q. processed the cryo-EM data. X.C. performed SEC-MALS, liposome-binding assays, leakage of liposome

contents assays, and single-channel current recording, and L.Z. supervised the analysis of the single-channel recordings. C.T. provided technical assistance with in situ experiments. L.L. conducted subcellular localization experiment, construction of knockout strain, and transcriptome sequencing analysis. C.W. performed label-free mass spectrometry experiments and analyzed data. All authors contributed to data analysis. X.C., W.G., and Z.H.Z. wrote the manuscript with assistance from all other authors. **Competing interests:** The authors declare that they have no competing interests. **Data and materials availability:** All data needed to evaluate the conclusions in the paper are present in the paper and/or the Supplementary Materials. In addition, the atomic structures of Rv3705c-SD and MSMEG_6251-SD have been deposited in the Protein Data Bank (PDB) under accession numbers 7CU8 and 7CU9, respectively. Cryo-EM maps of Rv3705c-FL with D_8 and C_1 symmetry have been deposited in the Electron Microscopy Data Bank (EMDB) under accession numbers EMD-22705 and EMD-22706, respectively.

Submitted 16 January 2021
Accepted 29 June 2021
Published 20 August 2021
10.1126/sciadv.abg5656

Citation: X. Cai, L. Liu, C. Qiu, C. Wen, Y. He, Y. Cui, S. Li, X. Zhang, L. Zhang, C. Tian, L. Bi, Z. H. Zhou, W. Gong, Identification and architecture of a putative secretion tube across mycobacterial outer envelope. *Sci. Adv.* **7**, eabg5656 (2021).